All-atom Molecular Dynamics Simulations of Cationic Polyelectrolyte Brushes In the Presence of Halide Counterions

Raashiq Ishraaq,[1] and Siddhartha Das[1]*

[1]Department of Mechanical Engineering, University of Maryland, College Park, MD 20742

*Email: sidd@umd.edu

TOC

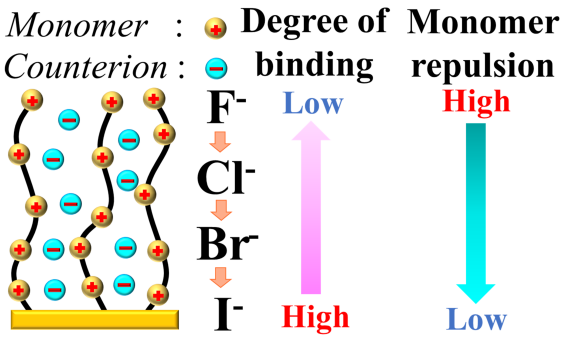

Abstract

Understanding the response of the charged polyelectrolyte (PE) brushes and brush-supported water and ions to the changes in the nature of screening counterions is significant in developing strategies for utilizing PE brushes in various applications. In this paper, we employ all-atom molecular dynamics (MD) simulations for studying the behavior of cationic [poly(2-(methacryloyloxy)ethyl) trimethylammonium] (PMETA) brushes and brush-supported water and ions in presence of different halide (X: I^-, Br^-, Cl^-, and F^-) screening counterions. We find that despite the F^- ion having the largest charge density, the extent of binding of the counterions on the PMETAX brushes vary as $I^- > Br^- > Cl^- > F^-$, leading to PMETAX brush height being least with I^- counterions and greatest with F^- counterions. This trend in the binding of the halide ions matches previous experimental result and can be explained by identifying the chaotropic nature of the I^- and Br^- ions that promote a disruption of water structure and a more favorable binding of the ions to the polymer chains. Such a binding trend also ensures that the order of the water molecules around the PMETAX chains or the counterions as well as the number of water-water hydrogen bonds inside the brush layer increase in the following order of the counterion-specific PMETAX brushes: $F^- > Cl^- > Br^- > I^-$. Furthermore, halide-ion-PMETAX-chain binding takes place *via* both interchain and intrachain bridging: intrachain bridging dominates for the case of counterions that show enhanced binding (I^- and Br^-), while interchain bridging is more favored for the case of counterions that show weakened binding (F^- and Cl^-). Also, a greater degree of intrachain bridging leads to a greater compressibility and flexibility of the brush layer. Finally, we show that the mobility of the halide ions follows a non-monotonic trend with the charge density: the mobility decreases as $I^- < Br^- < Cl^-$ (as their binding to the PMETAX chains varies as $I^- > Br^- > Cl^-$), but the mobility of F^- ions is in between that of I^- and Br^- ions. We argue that the strongly attached

hydration layer and the ensued friction inside the brush layer leads to such a reduced mobility of the F^- ions.

INTRODUCTION

Densely grafted polymer and polyelectrolyte (PE) chains that form "brush"-like architecture[1-12] show excellent responsiveness to environmental-stimuli leading to their applications in protein analysis and purification,[13] fabricating surfaces with desired properties (e.g., lubricating surfaces,[14,15] surfaces with desired wettability,[16] anti-fouling surfaces,[15] etc.), membranes,[17] current rectifiers,[18] nanofluidic electrokinetic energy generators,[19-22] developing functionalized nanoparticles for targeted drug delivery,[23,24] oil recovery,[25] colloid stabilization,[26] and water harvesting,[27] and many more. One of the important elements of such stimuli sensitivity of the brushes is their ion-specific responses. For example, uncharged polymer brushes and charged PE brushes have shown a variety of responses depending on the nature of the salt present in the medium as well as the nature of screening counterions (for the case of the PE brushes). For example, in presence of multivalent screening counterions (e.g., Ca^{2+}, Mg^{2+}, Y^{3+} ions) PE brush layers have demonstrated extensive shrinking behavior,[28-38] reduced lubricity,[37] formation of inhomogeneous lateral structures,[36] improved regulation of nanofluidic electroosmotic transport,[39] etc. Similarly, cationic PE brushes have demonstrated distinct swelling behavior in presence of halide ions (I^-, Br^-, Cl^-, and F^-)[40] and Hoffmeister anions.[41] Furthermore, simulation results have demonstrated distinct effects of the variation of the nature of the monovalent alkali cations (Li^+, Na^+, K^+, and Cs^+)[42,40] and Hoffmeister cations[41] on the swelling behavior of the anionic brushes. A recent study by Kou *et al.*[41] has shown that cationic poly(2-(methacryloyloxy)ethyl) trimethylammonium (PMETA) brushes exhibit more ion specificity than anionic brushes. In another related study, Ji *et al.*[40] employed quartz crystal microbalance and dielectric spectroscopy and showed that the counterions are more strongly bound to the PSS (poly-styrene sulfonate) chains than PMETA chains.

The behavior of water-swollen polymer and PE brushes have been typically probed using theory,[43-48] coarse-grained molecular dynamics (MD) simulations,[49-57] and experiments.[29,32,36,37] These approaches have been useful in unraveling a variety of different issues concerning polymer and PE brushes (including their salt and ion-specific behaviors); however they are incapable of providing an atomistic picture (of such brush-water-ion systems) that will be able to identify the effect of each atom of the polymer and PE system on the properties of the brushes and brush-supported ions and water molecules. Only recently, such polymer and PE brushes, as well as brush-supported water molecules and salt ions have been started to be probed atomistically by the use of all-atom MD simulations. Some of these investigations include studying the behavior of uncharged poly-ethylene glycol brushes and brush-supported water molecules,[58-60] behavior of anionic poly-acrylic acid (PAA) and poly-styrene sulfonic (PSS) brushes and brush-supported water molecules and ions in presence of monovalent[61,62] and multivalent counterions,[63] electric field,[64] nanoconfinement,[19,65] and temperature changes,[66] behavior of cationic PMETAC brushes and brush-supported water and ions in presence of screening chloride counterions,[67,68] etc. Unlike the cases of anionic brushes, the atomistic scale behavior of the cationic brushes has been less explored, especially the screening-counterion-specific responses of such cationic brushes.

In this paper, we employ all-atom MD simulations to probe for the first time the ion-specific response of the cationic PMETAX brushes: specifically, we study the response of the PMETAX brushes and the brush-supported water molecules and ions in presence of different halide (X: I^-, Br^-, Cl^-, and F^-) counterions. Here PMETA refers to [poly(2(methacryloyloxy)ethyl) trimethylammonium], which is the polymer chain. Now if the counterion is Cl^- (chloride), it is called [poly(2-(methacryloyloxy)ethyl) trimethylammonium *chloride*] or in short form PMETAC. If we are referring to samples of PMETA brushes screened by different halide counterions, in

short, we call it PMETAX, where "X" is the generic halide ion (i.e., X=F^- or Cl^- or Br^- or I^-). Our simulations reveal that the iodide (fluoride) ions show the maximum (minimum) extent of binding to the PMETAX brushes, despite the iodide (fluoride) ions having the minimum (maximum) charge density. This anomaly, which leads to the brush height being the smallest (largest) in presence of the iodide (fluoride) screening counterions and is also confirmed by recent experiments,[40] can be explained by noting the chaotropic (kosmotropic) nature of the iodide (fluoride) ions that enable the iodide (fluoride) ions to disrupt (bind favorably with) the water molecules and bind more (less) favorably with the PMETAX chains. Also, the ions with weaker (greater) charge density promote intrachain (interchain) bridging of the PMETAX monomers; accordingly, the PMETAX layers show greater flexibility and compressibility for the ions with weaker charge density (I^-, Br^- ions). Furthermore, the preferred binding of the I^- and Br^- ions on the PMETAX chains ensures that the water molecules in the vicinity of the PMETAX chains are less structured for the case of the PMETAX brushes screened I^- and Br^- counterions. Finally, we identify that the strongly condensed solvation shell of the F^- ion leads to non-monotonic size dependent variation of the halide ion mobility, with mobility varying as $I^- < F^- < Br^- < Cl^-$.

METHODS

We performed all-atom MD simulations of water-solvated PMETAX brush systems. We considered separate cases of the PMETAX brushes screened with different halide counterions (X: I^-, Br^-, Cl^-, and F^-). For each case, we considered a brush grafting density of 0.25 chains/nm^2. Such a grafting density value is in the range reported in previous experimental studies.[69,70] Each PMETAX chain consisted of 24 monomers and had two methyl group cappings at the end of the chain. The chains were arranged in a 5 x 5 square array and were solvated in water: Fig. 1(a) provides a snapshot of the system. OPLS-all-atom[71] forcefield was used to model the interactions between the atoms of the PMETAX chains; such force fields were previously used to model PMETAX chains.[67,68] For water, we used the SPC/E water model;[60] this model, when used with the OPLS-AA forcefield, showed excellent reproducibility of the polymer properties that match closely with those observed experimentally. Furthermore, while geometric rules were applied to determine the Lennard Jones (LJ) interaction parameters for dissimilar atoms of the PMETAX brush, an exception was made for ion-ion and ion-water LJ interactions. For these cases, similar to the approach of Chetham *et al.*,[72] the Lorentz-Berthelot mixing rule was used. In section S1 of the SI (Supporting Information), we have provided the forcefield parameters used for modeling the different interactions considered in this study. Periodic boundary conditions were applied in *x* and *y* directions, while a fixed boundary condition was applied along the *z* direction.

With regards to the simulation procedure, at first energy minimization was carried out to remove any overlap among the particles. Subsequently, the system pressure was equilibrated to 1 atmosphere using the NP_zT ensemble using Nosé-Hoover thermostat and barostat. Then the system was equilibrated in an NVT ensemble using the Langevin thermostat. Finally, the production run (20 ns) was carried out using the NVT ensemble. During the production run, we used the Langevin

thermostat except for the case of calculating ion mobilities, where we used Nosé-Hoover thermostat for better prediction of the relevant parameters.[61] The relaxation times for the thermostat and the barostat were 0.1 ps and 1 ps, respectively.[61] Long ranged Columbic forces were calculated using the PPPM (particle-particle particle-mesh) algorithm with 10^{-4} relative accuracy.[61] Time integration was performed with a timestep of 2 fs using the Velocity Verlet algorithm.[61] The bonds and angle of the water molecules were fixed using the SHAKE algorithm.[66] A detailed description of the equilibration time as well as the equilibration criteria that we have used here (*via* checking the autocorrelation function of the average brush height, see Fig. S2 in the SI) has been discussed in details in our previous article.[68] All simulations were carried out using the LAMMPS software package.[73] For visualization and illustration purposes we used OVITO[74] and Avogadro software.[75] Finally, for making the initial structure we used the MOLTEMPLATE package.[76]

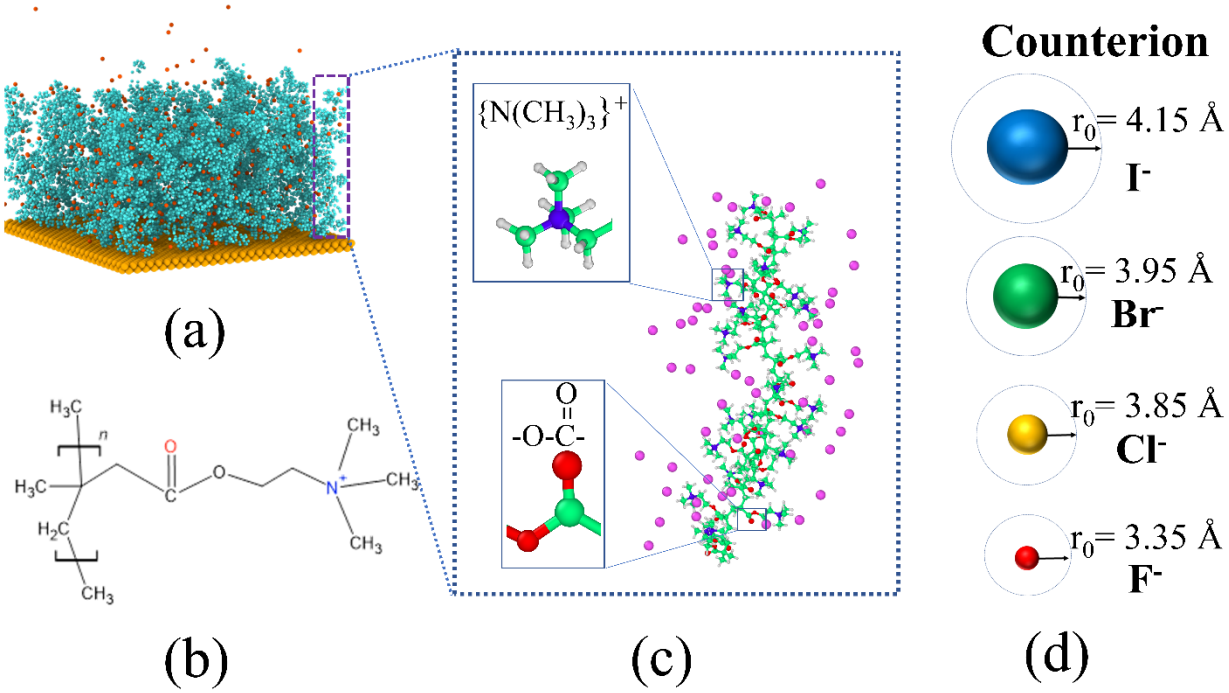

Figure 1. (a) A schematic of the brush system. The cyan, red, and orange spheres respectively denote the brush monomers, counterions, and wall atoms. (b) Chemical structure of the monomer. (c) A detailed structure of the polymer chain and the functional groups. Green, white, red, blue, and purple spheres respectively denote the carbon, hydrogen, oxygen, nitrogen, and halide counterions. (d) Representation of the size of the different halide counterions and their solvation shells.

RESULTS AND DISCUSSIONS

Effect of halide counterions on brush properties

Here we first study the interactions between the brushes and the halide ions. For that purpose, we first quantify the radial distribution function (RDF) between the $\{N(CH_3)_3\}^+$ group (the charged functional group of the PMETAX chains) and the halide ions [see Fig. 2(a)]. This RDF will provide the information on the extent of binding between the halide ions and the $\{N(CH_3)_3\}^+$ group (or the PMETAX chains). In the light of direct ion binding, it is expected that the ion with the highest charge density (in this case, F^- ion) will be most strongly condensed on the brush [or the $\{N(CH_3)_3\}^+$ group] followed progressively by the ions with the lesser charge densities. However, in this case we observe just the opposite trend: the degree of condensation varies as $I^- > Br^- > Cl^- > F^-$. This specific trend in the degree of condensation can be noted from the fact that the magnitude of the 1st peak in the $\{N(CH_3)_3\}^+$-X (X= I^-, Br^-, Cl^-, and F^-) RDF decreases in the order of $I^- > Br^- > Cl^- > F^-$ [see Fig. 2(a)]. Furthermore, such a trend in condensation has also been reported in the experimental study of Ji *et al.*[40] We believe that this trend is consistent with the kosmotropic/chaotropic picture of ion solvation. Kosmotropic ions tend to interact favorably with water, while the chaotropic ions do the opposite[41]. Experimentally, it has been validated that the F^- and Cl^- ions are in the kosmotrope side (Cl^- ion is at the boundary between the kosmotrope and chaotrope sides), while the Br^- and I^- ions are in the chaotrope side of the Hoffmeister series[77]. As the ions become more chaotropic (i.e., disrupt the nearby water structure), the ions tend to condense more favorably on nearby PE chains[40]. Later we show (see Fig. 4 and related discussion) that the level of hydration of the $\{N(CH_3)_3\}^+$ moiety of the PMETAX chains, very much like the Br^- and I^- ions, is weak. As a result, according to Collin's law of matching water affinity,[78] $\{N(CH_3)_3\}^+$ moiety and the halide ion (Br^- or I^-) are able to disrupt their respective hydration

layers and form stronger $\{N(CH_3)_3\}^+$-Br^- or $\{N(CH_3)_3\}^+$-I^- ion-pairs. This explains the reason for which the I^- and Br^- ions show a greater tendency to condense on the PMETAX chains [or the $\{N(CH_3)_3\}^+$ group of the PMETAX chains] as compared to the F^- and Cl^- ions, despite the charge densities increasing as $F^- > Cl^- > Br^- > I^-$.

Depending on the degree of condensation, the properties of the brush structure vary significantly. Fig. 2(b) shows the variation of the average PMETAX brush height for the cases of the PMETAX brushes screened with different counterions. It is expected that the counterions with the largest charge density will lead to the strongest screening of the PMETAX brushes: such screening will significantly reduce the intersegmental repulsion leading to the smallest brush height. However, in this case, we find that the brush height is much larger for the case of the F^- screening counterions (i.e., halide ions with the greatest charge density), and much smaller for the case of the I^- screening counterions (i.e., the halide ion with the least charge density), which is a result of this reverse order of counterion condensation ($I^- > Br^- > Cl^- > F^-$). Greater condensation implies greater extent of screening the PMETAC monomer charges leading to the maximum reduction of the PMETAC brush height. This effect of the halide-ion-specific condensation driven brush height reduction is manifested in the corresponding dimensionless monomer distribution of the PMETAC brushes [see Fig. 2(c)]. As the brush height is smallest for the case of PMETAC brushes screened with iodide counterions, we find that the monomer density starts to decay (indicating the end of brush height) from a smaller z value for this case. On the other hand, the larger brush height for the case of the PMETAC brushes with screening fluoride ions implies that the monomer density starts to decay from a larger z value. Fig. 2(d) shows the probability distribution of the location of the end monomer of the PMETAX brushes for the different cases considered here. Given the substantially reduced height for the case of the iodide-ion-screened PMETAX brushes, the maximum

probability of finding the end monomer (of the corresponding PMETAX brushes) is at a reduced z value. On the other hand, the enhanced height of the fluoride-ion-screened PMETAC brushes ensures that the maximum probability of finding the corresponding end monomer is at a much larger z value. Finally, near similar brush height values of the chloride-ion-screened and bromide-ion-screened PMETAX brushes ensures that the probability of finding the end monomers of the corresponding PMETAX brushes is at similar z values.

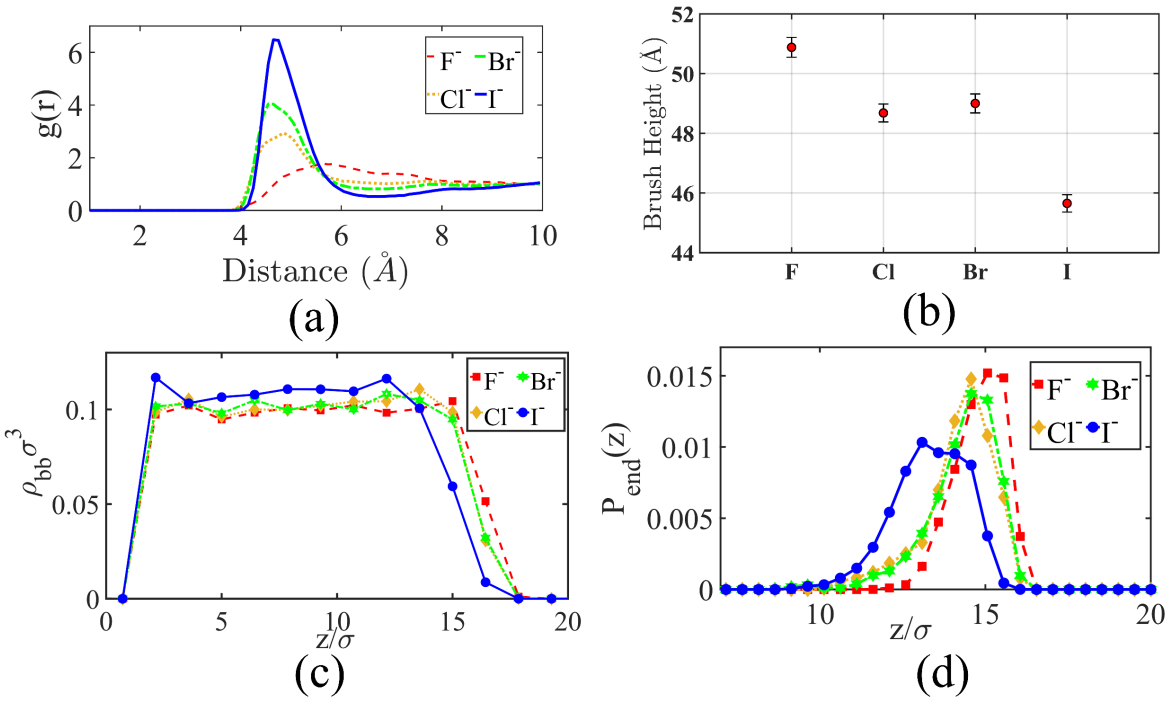

Figure 2. (a) RDF of $\{N(CH_3)_3\}^+$-X (X= I^-, Br^-, Cl^-, and F^-). (b) PMETAX brush height variation. (c) PMETAX brush backbone monomer distribution with *z*. (d) End chain monomer distribution with *z*. In (b-d), results have been shown for the cases where the PMETAX brushes have been screened with different halide counterions. Here σ=3.5 Å.

We further investigated the more detailed mechanism responsible for the brush height reduction for the case of different screening halide ions. When ions condense on a PE chain, they can induce two types of bridging effects: interchain bridging and intrachain bridging. Interchain bridging occurs when the functional groups of *two different PE chains* are in the solvation shell of a particular counterion; on the other hand, intrachain bridging occurs when functional groups of the *same chain* are present in the solvation shell of the counterion. A schematic of these two types of bridging has been provided in Fig. 3(a). In real systems, a mixture of these two types of bridging occurs. We calculated the ability (in percentage) of the different halide counterions to induce these two types of bridging [see Figs. 3(b) and 3(c)]. The details of the procedure used for calculating such bridging have been provided in section S3.5 and Fig. S3 in the SI. It can be seen that as the extent of ion condensation on the PMETAX chain increases in the order I^-> Br^- > Cl^- > F^-, the extent of the intrachain bridging increases [see Fig. 3(b)], but the extent of the interchain bridging decreases. When ions condense more on the chain (e.g., I^- counterions), the interchain repulsion decreases; as a result, the flexibility (springiness) of the brush structure increases. This can also be observed from the increasing width of the end chain probability distribution [see Fig. 2(d)]. The width denotes movement of the chain end along z direction: greater the *z* span, larger is the flexibility of the chain (in *z* direction). Such enhanced flexibility (in *z* direction) also ensures that the chain can collapse vertically more extensively, as evident from the reduced PMETAX brush height for the case of I^- screening counterions. Furthermore, such collapse (or height reduction) ensures that the functional groups of the same chain come closer to one another, thereby increasing the propensity of the intrachain bridging. On the other hand, when the ion condensation on the polymer chains is weak, interchain repulsion is high and the ability for the chains to fluctuate vertically (in the z direction) is less. Accordingly, two

adjacent chains show a greater tendency to fluctuate laterally than to fluctuate vertically; under such circumstances, the functional groups from these adjacent chains can simultaneously access the solvation shell of a counterion positioned in the vicinity of these two chains. This ensures that the propensity of interchain bridging increases: therefore, the interchain bridging increases in the order F^-> Cl^- > Br^- > I^- [see Fig. 3(c)], i.e., in the reverse order in which the extent of counterion condensation increases (i.e., I^-> Br^- > Cl^- > F^-). Also, a greater flexibility in z direction or a greater extent of fluctuations in z direction (or equivalently, an enhanced elasticity in z direction) of the PMETAX brushes, occurring in the same order as that of the extent of condensation (I^-> Br^- > Cl^- > F^-) on these brushes, ensures that the compressibility factor (β) of these chains also increases in the same order (I^-> Br^- > Cl^- > F^-) [see Fig. 3(d)]. Please note that the compressibility factor is defined in eq.(1) (with k_BT being the thermal energy and V being the volume of the brush layer): this factor depends on the square of the volume fluctuation ($\langle \Delta V \rangle$), and therefore increases nonlinearly with ion condensation[79].

$$\beta = \frac{1}{k_BT}\frac{\langle \Delta V \rangle^2}{V}. \quad (1)$$

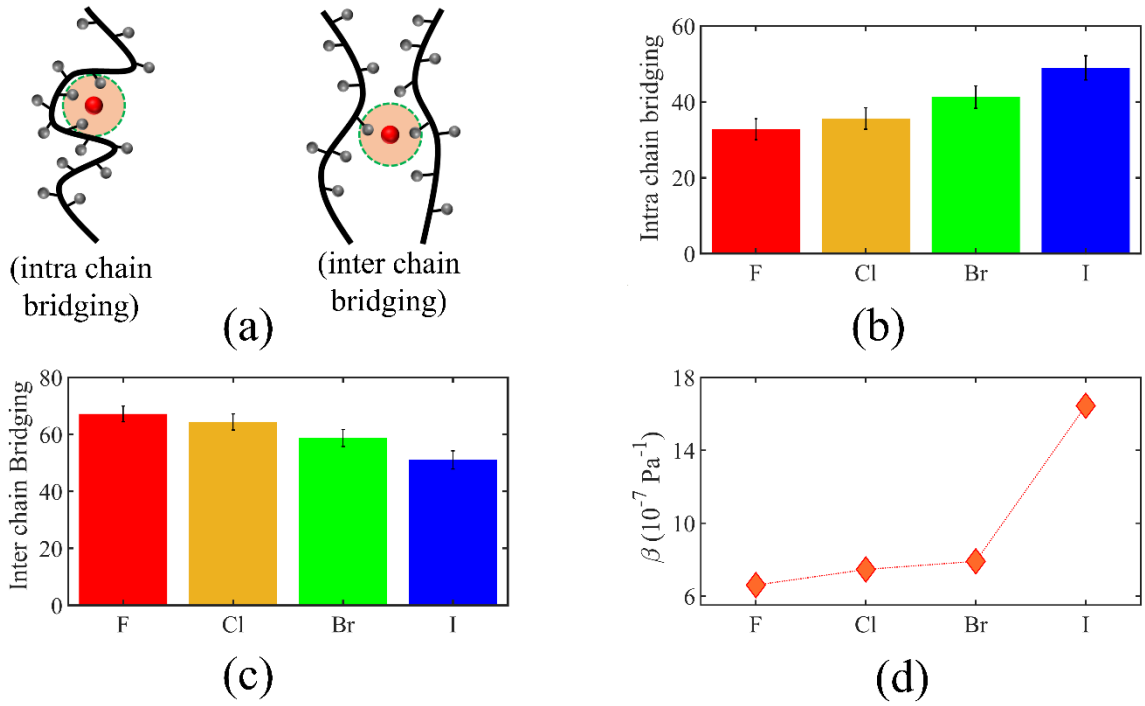

Figure 3. (a) A schematic of two types of bridging interactions: intrachain bridging and interchain bridging. (b) Percentage of intrachain bridging undergone by the monomers of the PMETAX chains. (c) Percentage of interchain bridging undergone by the monomers of the PMETAX chains. (d) Variation of the compressibility factor of the PMETAX chains forming the brush layer. In (b-d), results have been shown for the cases where the PMETAX brushes have been screened with different halide counterions.

Effect of halide counterions on water microstructure:

The different screening halide counterions interact with the PMETA PE chain by forming ion pairs.[40] The behavior of the ion pair, discussed in details in Refs. 79-81, is dictated by the interplay of the participating ions as well as their solvating water molecules [a schematic has been shown in Fig. 4(a)]. Therefore, understanding the properties of the water of these ion pair is important in deciphering the physics of the phenomenon. Furthermore, in the study conducted by Ji et al.[40], following the validation of the trend of counterion condensation, they advocated for a detailed examination of ion-pair behavior to gain a microscopic perspective for deciphering the underlying mechanism. Fig. 4(b) provides the X-O_w RDF inside the PMETAC brush layer (X: F^-, Cl^-, Br^-, and I^-; O_w: oxygen atom of the water molecule). These RDFs signify the affinity for water molecules of the different halide ions. The fluoride ion has the largest charge density and accordingly its degree hydration is the highest, followed by the chloride, bromide, and iodide ions: this trend is commensurate with the fact that the charge density progressively decreases from fluoride to chloride to bromide to iodide ions). Such enhanced hydration, of course, can be inferred by noting that the value of the 1st peak of the X-O_w RDF is highest for the fluoride ion followed by the chloride, bromide, and iodide ions. In Fig. 4(c), we study the water dipole orientation around the counterions inside the brush layer by quantifying the probability distribution of the water dipole orientation angle, θ. Consistent with the hydration picture, one can see that due to the highest charge density, the fluoride ion manages to orient the water molecules to the largest extent (as manifested by a narrower and steeper probability distribution of the dipole angle θ), followed by the chloride, bromide, and iodide ions. The RDF and the dipole orientation signify that the hydration strength of the halide ions vary as $F^- > Cl^- > Br^- > I^-$. Fig. 4(d) provides the probability distribution of the tetrahedral order (q) of solvating water around the $\{N(CH_3)_3\}^+$ moiety [see

section S3.1. in the SI for the detailed calculation procedure employed to obtain *q*]. Smaller the *q* value (as compared to 1), more disrupted is the water structure from the classical tetrahedral structure. Fig. 4(d) shows that the extent of the disruption of the tetrahedral structure of water around the $\{N(CH_3)_3\}^+$ moiety varies in the same order as the extent of counterion condensation (i.e., $I^- > Br^- > Cl^- > F^-$). To find the origin of such disruption we also plotted the *q* parameter of the solvating water molecules around different halide ions. The water tetrahedral order is largest for the case of the F^- ion and the order varies as $F^- > Cl^- > Br^- > I^-$ [see Fig. 4(e)]. Such a trend is consistent with the kosmotropic/chaotropic picture of ion solvation.[41,82] Kosmotropic ions tend to interact favorably with water by disrupting the water-water structure less, while the chaotropic ions do the opposite. Experimentally, it is also validated that the F^- and the Cl^- ions are in the kosmotrope side (although Cl^- ion is in the boundary of kosmotrope), while the Br^- and the I^- ions are in the chaotrope side of the Hoffmeister series[77]. Moreover, the fact that the halide ions maintain their kosmotropic/chaotropic nature inside the brush elucidates the reason for this trend of the degree of condensation ($I^- > Br^- > Cl^- > F^-$) of the halide ions on the PMETAX brushes [as described in Fig. 2(a)]. According to Collin's law of matching water affinity (LMWA), kosmotropic ions have high water affinity (strongly hydrated) and tend to form strong ion-pair with other kosmotropic ions.[78,83] On the other hand, chaotropic ions are weakly hydrated and tend to form strong ion pair with other chaotropic ions.[78,83] In a solution, ion pairing becomes strong when the affinity towards water molecule of both ions is similar (i.e., the case of *like attracts like*): under such circumstances, the ion-ion interaction strength becomes large enough to overcome the barrier created by the hydration shells of both the ions.[78,83] In our previous paper,[68] we have shown that the $\{N(CH_3)_3\}^+$ moiety of the PMETA chain acts as a weakly hydrated entity and undergoes an apolar hydration. For the present case, as the counterions are changed from F^- to I^-, the

counterions become more chaotropic (weakly hydrated) [as evident from Figs. 4(a), 4(b), and 4(d)] and as a result the degree of condensation to the weakly hydrated $\{N(CH_3)_3\}^+$ moiety increases.

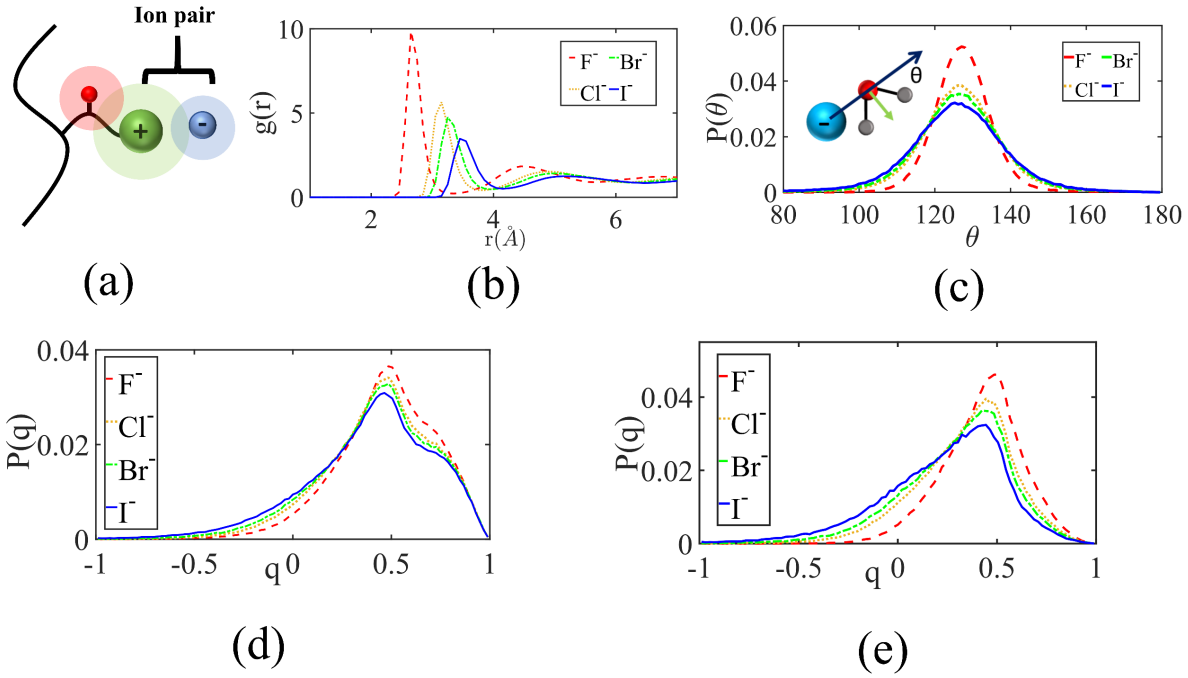

Figure 4: (a) A schematic of the ion pair inside the PMETAX brush. The green, blue, and red transparent zones represent the hydration layers around the cation, the anion, and the $\{N(CH_3)_3\}^+$ moiety (of the PMETAX chain), respectively. (b) X-O_w RDF inside the PMETAX brush layer (X: F^-, Cl^-, Br^-, and I^-; O_w: oxygen atom of the water molecule). (c) Distribution of the dipole orientation angle (θ) of the solvation water for different halide ions inside the PMETAC brush layer. In the inset of this figure, we provide a schematic description of this angle θ. In this schematic, the blue sphere represents the anion, while the red and the grey spheres represent the water and hydrogen atoms of the water molecule. (d) Tetrahedral order parameter (q) of the solvating water of $\{N(CH_3)_3\}^+$ moiety. (e) Tetrahedral order parameter (q) of the solvating water of the halide counterions inside the PMETAX brush layer. In (b-e), results have been shown for the cases where the PMETAX brushes have been screened with different halide counterions.

We also investigated the overlap of the solvation shell of different moieties inside the brush system. Fig 5(a) provides a pie chart showing the percentage of solvation shell water molecules of the $\{N(CH_3)_3\}^+$ moiety of the PMETA-F chain that is shared between different moieties of the PMETA-F system (see section S4 and Fig. S4 in the SI for the equivalent results for PMETA-Cl, PMETA-Br, and PMETA-I systems). The percentage of shared water between the halide ion and $\{N(CH_3)_3\}^+$ increases in the same order as the extent of condensation ($I^- > Br^- > Cl^- > F^-$) [see Fig. 5(b)]. To investigate the effect of different counterions on the overall solvation of the brush system, we plotted the dimensionless water density inside and outside the PMETAX brush layer [see Fig. 5(c)]. The water density is always smaller inside the brush layer since inside the brush layer, given the presence of the brush monomer and counterions, there is a lesser space for the water molecules to reside. This behavior has been found for other types of brushes as well[62]. When the cases of the different screening counterions are compared, we find that the water density (inside the brush layer) is least (highest) for the case of iodide (fluoride) screening counterions. This can be justified by noting that the size of the iodide (fluoride) ion is largest (smallest), providing least (highest) space for the water molecules to reside inside the brush layer, causing a reduced (enhanced) water density inside the brush layer. This phenomenon indicates that the PMETAX brushes are subjected to two opposing effects when the sizes of the screening counterions are varied. When ion size is increased ($I^- > Br^- > Cl^- > F^-$), the ion becomes more chaotropic and as a result condenses more favorably in the brush and lowers the interchain repulsion. However, as we increase the counterion size, lesser water will be available inside the brush layer. Since water is a polar solvent, it also acts as a dielectric medium causing a reduction in the intersegmental charge among the chains: therefore, a reduction in water density enhances (due to the dielectric nature of water) the intersegmental repulsion. Therefore, when the screening halide counterion sizes are increased,

there are two opposing effects on PE chain repulsion: (1) a reduced chain-chain repulsion due to enhanced counterion condensation and (2) an enhanced chain-chain repulsion due to depletion of water. Various results (including the brush height) show relatively less difference between the cases of chloride and bromide counterions. The presence of these two above-discussed counterion-size-dependent competing effects (causing a variation in the intersegmental repulsion) might be the reason for such an occurrence. Finally, we also calculated, the hydrogen bond number (n_{Hbond}) distribution for different PMETAX system. Though the n_{Hbond} remains mostly similar for all the systems, there is a slight decrease for larger counterions [compare the corresponding cases between the F^- and I^- counterions in the inset of Fig. 5(d)]. Of course, the strength the water-water hydrogen bonds for all the systems (PMETAX system with different halide screening counterions) remain the same (see section S5 in the SI for more details).

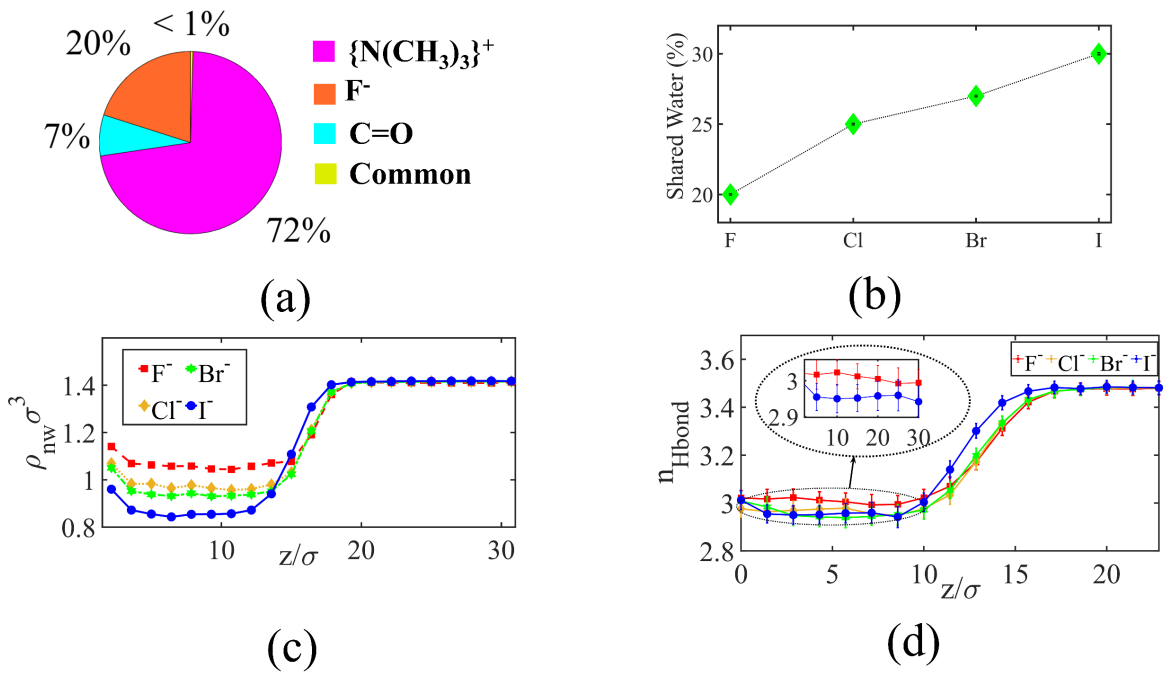

Figure 5: (a) A piechart showing the percentage of solvation shell water of the $\{N(CH_3)_3\}^+$ moiety (of the PMETA-F system) that are shared between different moieties of the PMETA-F system. (b) Solvation water (in percentage) of the $\{N(CH_3)_3\}^+$ moiety that is shared with halide ions for the different PMETAX system (X: F^-, Cl^-, Br^-, and I^-). Maximum uncertainty in the different curves is 0.0697. (c) Variation in the water number density inside the PMETA-X brush layer. (d) Variation in the hydrogen bond number distribution inside the PMETA-X brush layer. In (b-d), results have been shown for the cases where the PMETAX brushes have been screened with different halide counterions.

Behavior of the Brush Supported Counterions

Next, we investigated various static and dynamical properties of the halide counterions. Fig. 6(a) shows the distribution of the different halide counterions inside the PMETAX brush layer. The dimensionless counterion density, $\rho_{ci}\sigma^3$, is nearly uniform inside the brush layer, stemming from the corresponding uniformity in the monomer distribution [see Fig. 2(c)]. Also, the density of the counterions inside the brush layer is greater for the iodide-counterion-screened PMETA brush layer as compared to the fluoride-ion-screened PMETA brush layer. This enhanced density is manifested through a larger uniform value of the counterion number density inside the brush layer and the number density decaying to a zero value at a much smaller z. Such enhanced (reduced) density of the screening counterions for the iodide-ion-screened (fluoride-ion-screened) PMETAC brushes stem from the fact that the same number of monomer charges need to be screened within a smaller (larger) PE brush volume as the height of the iodide-ion-screened (fluoride-ion-screened) PMETAX brushes is smaller (larger). Fig. 6(b) provides the screening efficiency or SE (associated with the screening of the PMETAX brush charges) by the different halide counterions: this is expressed in terms of the percentage of the total PMETAX charge screened by the screening halide counterions inside the brush layer (see section S3.3. in the SI for the detailed calculation procedure). The results, which are obtained by averaging over time, show near complete screening of the PMETAX charges by the counterions for all the different cases of the halide counterions. This confirms that the halide screening counterions do not typically leave the PMETAX brush layer, suggesting a stable interaction between the counterions and the PMETAX brushes. We next investigate the mobility of counterions inside the brush layer. For this purpose, we calculated the MSD (mean square displacement) of these different screening counterions inside the brush layer [see Fig. 6(c)]. We used the Nosé-Hoover thermostat for calculating dynamic properties (e.g.,

MSD of the counterions) as it provided a greater accuracy[84]. Also, we calculated these dynamic properties using Langevin thermostat and the qualitative trend matches well with that predicted using the Nosé-Hoover thermostat (See section S6 and Figs. S6 in the SI). In this case, we see that except for the fluoride ion, the mobility of all other halide ions follows the trend predicted by their degree of binding to the PMETAX chains: their degree of binding varies as $I^- > Br^- > Cl^-$, and hence their mobility (or MSD) varies as $I^- < Br^- < Cl^-$. To investigate further, we calculated the probability mass function of the distance travelled by a counterion for 40 ps [see Fig. 6(d)]. It also shows that except for the fluoride ion, all other halide ions follow the trend that is commensurate with their extent of binding ($I^- > Br^- > Cl^-$), i.e., the extent of displacements undergone by these different ions vary as $I^- < Br^- < Cl^-$ [see Fig. 6(d) and its inset].

The mobility of a counterion in a porous medium is influenced by various factors: mass of the counterion, properties of the medium, strength of the solvation shell, interaction between medium and counterion, etc. Lighter mass and lesser degree of condensation on the PMETAX chain suggests that the F^- ion should have the highest mobility inside the PMETAX brush layer. However, the solvation shell of F^- ion is strong, which suggests that the water molecules are strongly bound to the F^- ion [see Fig. 4(b)]. This is further established by the corresponding free energy of binding (see section S3.2. in the SI for the calculation procedure) of water to a halide ion [see Fig. 7(a)] and the residence time (or equivalently, the survival probability or SP; see section S3.4. in the SI for the calculation procedure of the SP) of the water molecules within the solvation shell of the halide ions [see Fig. 7(b)]: both these results confirm that the water molecules are most strongly bound to the F^- ion and are most stable inside the F^- ion solvation shell. The environment inside the brush is similar to that inside a porous medium and it was previously reported that an ion with a strong and highly stable solvation shell experiences significant friction

during its migration inside a porous medium,[85] thereby decreasing its mobility. This is exactly the case for the fluoride ion inside the PMETAX brush layer. Having a strong and stable solvation shell counters the effect of smaller mass and weaker binding tendency of the F^- ion, thereby reducing its overall mobility. Accordingly, the mobility of the F^- ion is lesser than that of the Cl^- and Br^- ions, but greater than that of the I^- ion: this explains the non-monotonic (with halide counterions sizes, or equivalently, halide counterion charge densities) trend in the variation of halide ion mobility inside the PMETAX brush layer.

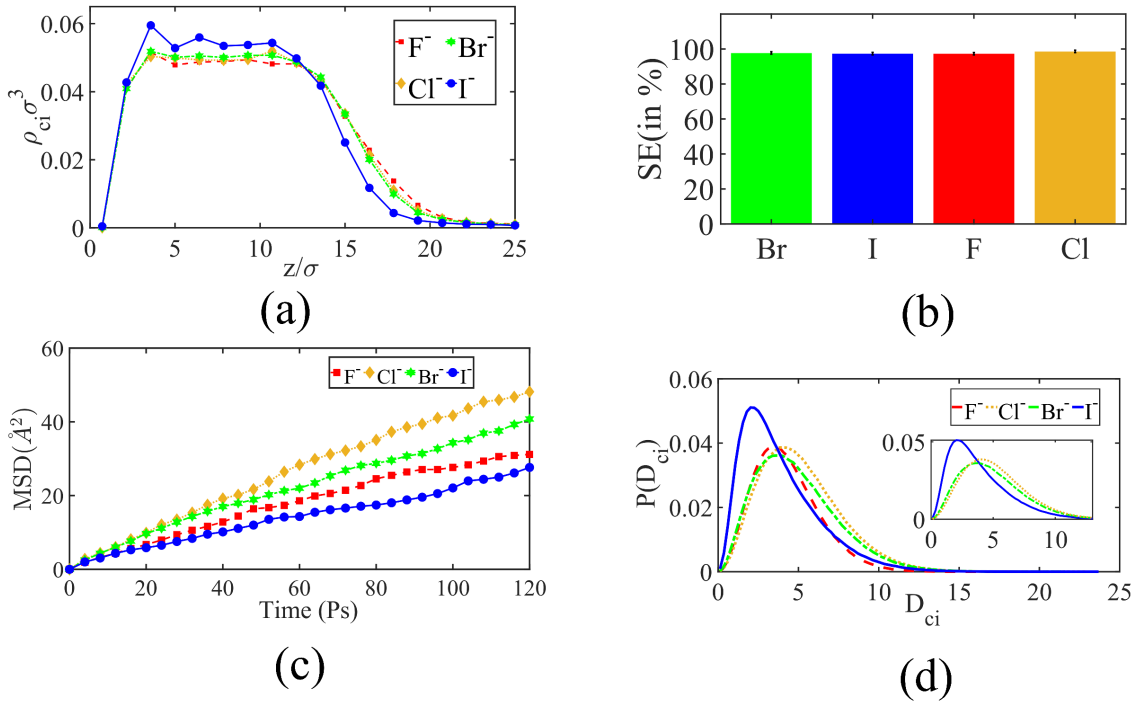

Figure 6. (a) Dimensionless number distribution (with *z*) of the different halide screening counterions. (b) Screening efficiency or SE (in screening the PMETAX brush charges) of the different halide screening counterions. (c) Mean square displacement of the different screening halide counterions inside the PMETAX brush layer (d) Probability mass function (PMF) of the distance travelled by a screening halide counterion (inside the PMETA brush layer) in 40 ps. In the inset of (d), the PMF of I^-, Br^-, and Cl^- have been provided for easier comparison.

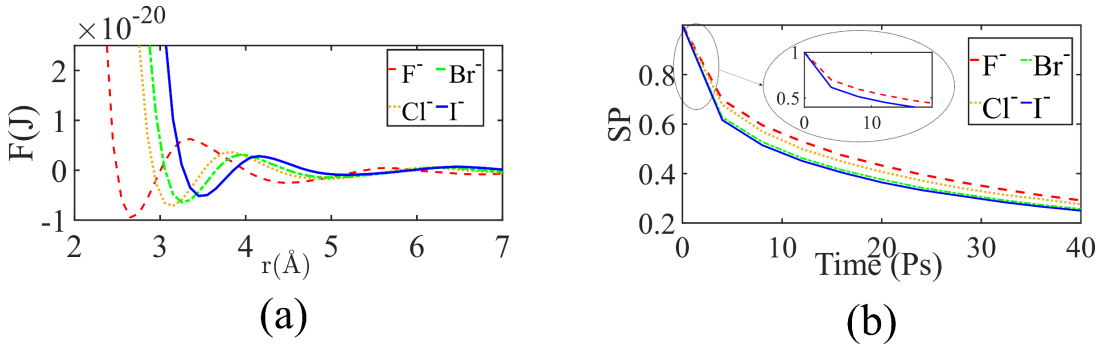

Figure 7. (a) Free energy of binding (in Joules/atom) between the halide ion and the oxygen of the water molecule. (b) Survival probability (SP) of water molecules inside the solvation shell of different halide ions.

CONCLUSIONS

In this article we conducted an all-atom molecular dynamics (MD) simulation with an explicit water model to explore the specific ion effects on densely grafted PMETAX brushes with halide counterions. Our findings indicate that the binding affinity of halide ions follows the sequence I^- > Br^- > Cl^- > F^-: this is a trend that is validated by experimental results.[40] Upon investigating the water structure surrounding the $\{N(CH_3)_3\}^+$ moiety of the PMETAX brush and the halide counterion, we uncovered that the binding affinity aligns with Collin's law of matching water affinity: in other words, as the counterion becomes more chaotropic (e.g., I^- and Br^- counterions) it binds more strongly to the weakly hydrated $\{N(CH_3)_3\}^+$ moiety. Furthermore, our study revealed that an increased ion binding to the PE chains reduces PE chain intersegmental electrostatic repulsion, leading to a decrease in the brush height and an increase in flexibility. This enhanced flexibility, resulting from increased ion condensation on the PE chain, is further associated with enhanced intrachain binding. At the same time, larger counterions (I^-, Br^-) decrease the water content inside the PMETAX brush layer due to increased excluded volume effects. This creates two mutually countering effects affecting the PMETAX intersegmental repulsion: (1) an enhanced intersegmental repulsion (for the case of the PMETAX chains screened with ions like I^- and Br^-) caused by the lowering of water acting as a dielectric medium and (2) a reduced intersegmental repulsion (for the case of the PMETA chains screened with ions like I^- and Br^-) due to enhanced binding of these ions with the PMETA chains. Finally, our results demonstrated that the mobility of counterions within the brush decreases with increased binding to the PE chain, with the exception of the F^- ion. This exception is attributed to the enhanced friction encountered by the F^- ion (inside the brush layer) due to its strongly attached hydration shell.

To summarize, our study not only explains the findings of a prior experimental study,[40] but also unveils new features of the PMETA-halide-ion systems. These insights can be leveraged in designing brushes with specific structural properties and ion mobility. This study also reveals the intricate microscopic features that emerge when altering ion sizes and charge densities. The study further points to a more complex scenario that will occur when one considers counterions with varying shapes, polarities, and hydrophobicities in such brush-like systems, emphasizing the need for further elucidation in future investigations.

Supporting Information

MD simulation details; Results on the time evolution and autocorrelation function of the PMETAX brush height; Procedure for the calculations of various parameters; Results on the Solvation shell composition of $\{N(CH_3)_3\}^+$ for PMETAX brushes screened with Cl^-, Br^-, and I^- ions; Results showing the hydrogen bond properties of brush confined water molecules; Results on the counterion mobility calculated with Langevin thermostat.

Acknowledgement: This work has been supported by the Department of Energy Office of Science grant DE-SC0017741. The authors also gratefully acknowledge the Zaratan High-Performance Computing cluster at the University of Maryland for providing necessary computational resources and Dr. Turash Haque Pial (former Ph.D. student of Dr. Siddhartha Das) for useful discussions.

References

1. Dadarlat,V. M.; Post, C. P. Insights into Protein Compressibility from Molecular Dynamics Simulations. J. Phys. Chem. B **2001**, *105(3)*, 715–724
2. Bhayo; A. M.; Yang, Y.; Xiangmin, H. Polymer brushes: Synthesis, characterization, properties and applications. *Prog. Mater. Sci.* **2022**, *130*, 10100
3. Van eck; G. C. R.; Chiapissi, L.; Beer, S. D. Fundamentals and Applications of Polymer Brushes in Air. A*CS Appl. Polym. Mater.* **2022**, *4(5)*, 3062–3087
4. Li, B.; Zhou, F.; Yu, B.; Sheng, W.; Wei, Q.; Wang, R. Driving Polymer Brushes from Synthesis to Functioning. *Angew. Chem. Int.* **2023**, *62(27)***,** 20221312
5. Zhou, F.; Yu, B.; Zhang, X.; Ma, S. Brushing up functional materials. *NPG Asia Mater.* **2019**, *11*, 24.
6. Milner, S. T. Polymer Brushes. *Science* **1991**, 251, 4996.
7. Yokoyama, H. New Developments in Polymer Brush Fabrication: Concepts and Physical Properties of Dynamic Polymer Brushes. *Polym. J.* **2023**, 55, 735-742.
8. Das, S.; Banik, M.; Chen, G.; Sinha, S.; Mukherjee, R. Polyelectrolyte Brushes: Theory, Modelling, Synthesis and Applications. *Soft Matter*, **2015**,*11*, 8550-8583
9. Schick, M.; Netz, R. R. Polymer Brushes: From Self-Consistent Field Theory to Classical Theory. *Macromolecules* **1998**, *31(15)*, 5105–5122
10. Xu, X.; Billing,M.; Ruths, M.; Klok, H.; Yu, J. Structure and Functionality of Polyelectrolyte Brushes: A Surface Force Perspective. *Chem. - Asian J.* **2018**, *13(22)*, 3411-3436.
11. Balauff, M.; Borisov, O. Polyelectrolyte brushes **2006**, *11(6)*, 316-323

12. Landes, C. F.; Reznik, C. Transport in Supported Polyelectrolyte Brushes *Acc. Chem. Res.* **2012**, *45(11)*, 1927–1935
13. Jain, P.; Baker, G. L.; Bruening, M. L. Applications of Polymer Brushes in Protein Analysis and Purification **2009**,*2*, 387-408
14. Bielecki, R. M.; Benetti, E. M.; Kumar, D.; Spencer, N. D Lubrication with Oil-Compatible Polymer Brushes *Tribol. Lett.* **2012**, *47*, 477-487
15. Yang, W.; Zhou, F. Polymer brushes for antibiofouling and lubrication *Biosurface and Biotribology*. **2017**, *3(3)*, 97-114.
16. Greve, D.; Hartmann, S.; Thiele, U. Stick-slip dynamics in the forced wetting of polymer brushes *Soft Matter,* **2023***,19,* 4041-4061.
17. Keating, J. J.; Imbrogno, J.; Belfort, G. Polymer Brushes for Membrane Separations: A Review *ACS Appl. Mater. Interfaces* **2016**, *8(42)*, 28383–28399.
18. Ali, M.; Yameen, B.; Cervera, J.; Ramírez, P.; Neumann, R.; Ensinger, W.; Knoll, W.; and Azzaroni, O. Layer-by-Layer Assembly of Polyelectrolytes into Ionic Current Rectifying Solid-State Nanopores: Insights from Theory and Experiment. *J. Am. Chem. Soc.* **2010**, *132(24)*, 8338–8348.
19. Sachar, H., S.; Pial, T., H.; Sivashankar, V. S.; Das, S. Simultaneous Energy Generation and Flow Enhancement (Electroslippage Effect) in Polyelectrolyte Brush Functionalized Nanochannels. *ACS Nano* **2021**, *15(11)*, 17337–17347.
20. Sachar, H.S.; Sivasankar, V.S.; Das, S. Electrokinetic energy conversion in nanochannels grafted with pH-responsive polyelectrolyte brushes modelled using augmented strong stretching theory. *Soft Matter*, **2019**,*15*, 5973-5986.

21. Chen, G.; Sachar, H. S.; Das, S. Efficient electrochemomechanical energy conversion in nanochannels grafted with end-charged polyelectrolyte brushes at medium and high salt concentration. *Soft Matter*, **2018**,*14*, 5246-5255

22. Patwary, J.; Chen, G.; Das, S. Efficient electrochemomechanical energy conversion in nanochannels grafted with polyelectrolyte layers with pH-dependent charge density. *Microfluid. Nanofluid.* **2016,** *20*,37.

23. Yang, Q.; Li, L.; Zhao, F.; Han, H.; Wang, W.; Tian, Y.; Wang, Y.; Ye, Z.; Guo, X. Hollow Silica-polyelectrolyte Composite Nanoparticles for Controlled Drug Delivery. *J. Mater. Sci.* **2019**, *54*, 2552−2565.

24. Saraswathy, M.; Gong, S. Recent Developments in the CoDelivery of siRNA and Small Molecule Anticancer Drugs for Cancer Treatment. *Mater. Today* **2014**, *17*, 298−306.

25. ShamsiJazeyi, H.; Miller, C. A.; Wong, M. S.; Tour, J. M.; Verduzco, R. Polymer-coated Nanoparticles for Enhanced Oil Recovery. J. *Appl. Polym. Sci*. **2014**, 131, 40576.

26. Motornov, M.; Sheparovych, R.; Lupitskyy, R.; MacWilliams, E.; Hoy, O.; Luzinov, I.; Minko, S. Stimuli-Responsive Colloidal Systems from Mixed Brush-Coated Nanoparticles. *Adv. Funct. Mater.* **2007**, *17*, 2307.

27. Liu, G.; Cai, M.; Wang, W.; Zhou, W.; Liu, W. Core–Shell–Corona-Structured Polyelectrolyte Brushes-Grafting Magnetic Nanoparticles for Water Harvesting. *ACS Appl. Mater. Interfaces* **2014**, *6(14)*, 11625–11632.

28. Yu, J.; Mao, J.; Yuan, G.; Satija, S.; Jiang, Z.; Chen, W.; Tirrell, M. Structure of Polyelectrolyte Brushes in the Presence of Multivalent Counterions. *Macromolecules* **2016**, *49*, 5609−5617.

29. Xu, X.; Mastropietro, D.; Ruths, M.; Tirrell, M.; Yu, J. Ion-Specific Effects of Divalent Ions on the Structure of Polyelectrolyte Brushes. *Langmuir* **2019**, *35*, 15564−15572.

30. Mei, Y.; Lauterbach, K.; Hoffmann, M.; Borisov, O. V.; Ballauff, M.; Jusufi, A. Collapse of Spherical Polyelectrolyte Brushes in the Presence of Multivalent Counterions. *Phys. Rev. Lett.* **2006**, *97*, 158301.

31. Xu, Y.; Bolisetty, S.; Drechsler, M.; Fang, B.; Yuan, J.; Harnau, L.; Ballauff, M.; Müller, A. H. E. Manipulating Cylindrical Polyelectrolyte Brushes on the Nanoscale by Counterions: Collapse Transition to Helical Structures. *Soft Matter* **2009**, *5*, 379−384.

32. Farina, R.; Laugel, N.; Yu, J.; Tirrell, M. Reversible Adhesion with Polyelectrolyte Brushes Tailored via the Uptake and Release of Trivalent Lanthanum Ions. *J. Phys. Chem. C* **2015**, *119*, 14805−14814.

33. Nap, R. J.; Park, S. H.; Szleifer, I. Competitive Calcium Ion Binding to End-tethered Weak Polyelectrolytes. *Soft Matter* **2018**, *14*, 2365−2378.

34. Ezhova, A.; Huber, K. Contraction and Coagulation of Spherical Polyelectrolyte Brushes in the Presence of Ag^{+}, Mg^{2+}, and Ca^{2+} Cations. *Macromolecules* **2016**, *49*, 7460−7468.

35. Jackson, N. E.; Brettmann, B. K.; Vishwanath, V.; Tirrell, M.; de Pablo, J. J. Comparing Solvophobic and Multivalent Induced Collapse in Polyelectrolyte Brushes. ACS Macro Lett. **2017**, *6*, 155−160.

36. Yu, J.; Jackson, N. E.; Xu, X.; Brettmann, B. K.; Ruths, M.; de Pablo, J. J.; Tirrell, M. Multivalent Ions Induce Lateral Structural Inhomogeneities in Polyelectrolyte Brushes. *Sci. Adv.* **2017**, *3*, No. eaao1497.

37. Yu, J.; Jackson, N. E.; Xu, X.; Morgenstern, Y.; Kaufman, Y.; Ruths, M.; de Pablo, J. J.; Tirrell, M. Multivalent Counterions Diminish the Lubricity of Polyelectrolyte Brushes. *Science* **2018**, *360*, 1434−1438.

38. Mei, Y.; Hoffmann, M.; Ballauff, M.; Jusufi, A. Spherical Polyelectrolyte Brushes in the Presence of Multivalent Counterions: The effect of Fluctuations and Correlations as Determined by Molecular Dynamics Simulations. Phys. Rev. E: Stat., Nonlinear, *Soft Matter Phys.* **2008**, *77*, 031805.

39. Pial, T.H.; Das, S. Specific Ion and Electric Field Controlled Diverse Ion Distribution and Electroosmotic Transport in a Polyelectrolyte Brush Grafted Nanochannel. *Phys. Chem. B* **2022**, *126(49)*, 10543–10553

40. Ji, C.; Zhou, C.; Zhao, B.; Yang, J.; Zhao, J. Effect of Counterion Binding to Swelling of Polyelectrolyte Brushes. *Langmuir* **2021**, *37(18)*, 5554–5562.

41. Kou, R.; Zhang, J.; Wang, T.; Liu, T. Interactions between Polyelectrolyte Brushes and Hofmeister Ions: Chaotropes versus Kosmotropes. *Langmuir* **2015**, *31(38)*, 10461–10468.

42. Ropero, F. R.; Vegt, N. F. V. D. Ionic Specific Effects on the Structure, Mechanics and Interfacial Softness of a Polyelectrolyte Brush. *Faraday Discuss.*, **2013**,*160*, 297-309.

43. Chen, L.; Merlitz, H.; He, S.; Wu, C. X.; Sommer, J. W. Polyelectrolyte Brushes: Debye Approximation and Mean-Field Theory. *Macromolecules* **2011**, *44*, 3109−3116.

44. Borisov, O. V.; Zhulina, E. B. Conformations of Polyelectrolyte Molecular Brushes: A Mean-Field Theory. *J. Chem. Phys.* **2018**, *149*, No. 184904.

45. Zhulina, E. B.; Wolterink, J. K.; Borisov, O. V. Screening Effects in a Polyelectrolyte Brush: Self-Consistent-Field Theory. *Macromolecules* **2000**, *33*, 4945−4953.

46. Okrugin, B. M.; Richter, R. P.; Leermakers, F. A. M.; Neelov, I. M.; Borisov, O. V.; Zhulina, E. B. Structure and Properties of Polydisperse Polyelectrolyte Brushes Studied by Self-Consistent Field Theory. *Soft Matter* **2018**, *14*, 6230−6242.

47. Sachar, H. S.; Sivasankar, V. S.; Das, S. Revisiting the Strong Stretching Theory for Ph-Responsive Polyelectrolyte Brushes: Effects of Consideration of Excluded Volume Interactions and An Expanded Form of The Mass Action Law. *Soft Matter* **2019**, *15*, 559−574.

48. Etha, S. A.; Sivasankar, V. S.; Sachar, H. S.; Das, S. Strong Stretching Theory for pH-Responsive Polyelectrolyte Brushes in Large Salt Concentrations. *Phys. Chem. Chem. Phys.* **2020**, *22*, 13536−13553.

49. Desai, P. R.; Wang, Y.; Sachar, H. S.; Jing, H.; Sinha, S.; Das, S. Supersolvophobic Soft Wetting: Nanoscale Elastocapillarity, Adhesion, and Retention of a Drop Behaving as a Nanoparticle. *Matter* **2019**, *1(5)*, 1262-1273.

50. Yuan, J.; Antila, S. H.; Luitjen, E. Structure of Polyelectrolyte Brushes on Polarizable Substrates. *Macromolecules* **2020**, *53*, 2983−2990.

51. Luo, Y.; Wang, C.; Pang, A.; Zhang, X.; Wang, D.; Lu, X. Low-Concentration Salt Solution Changes the Interfacial Molecular Behavior of Polyelectrolyte Brushes. *Macromolecules* **2021**, *54*, 6006−6013.

52. Elliott, I. G.; Kuhl, T. L.; Faller, R. Molecular Simulation Study of the Structure of High Density Polymer Brushes in Good Solvent. *Macromolecules* **2010**, *43*, 9131−9138.

53. Lo Verso, F.; Egorov, S. A.; Milchev, A.; Binder, K. Spherical Polymer Brushes Under Good Solvent Conditions: Molecular Dynamics Results Compared to Density Functional *Theory. J. Chem. Phys.* **2010**, *133*, No. 184901.

54. Smook, L. A.; van Eck, G. C. R.; de Beer, S. Friends, Foes, and Favorites: Relative Interactions Determine How Polymer Brushes Absorb Vapors of Binary Solvents. *Macromolecules* **2020**, *53*, 10898−10906.

55. Mensink, L. I. S.; de Beer, S.; Snoeijer, J. H. The Role of Entropy in Wetting of Polymer Brushes. *Soft Matter* **2021**, *17*, 1368−1375.

56. Glišić, I.; Eck, G. C. R. V.; Smook, L. A.; de Beer, S. Enhanced Vapor Sorption in Block and Random Copolymer Brushes. *Soft Matter* **2022**, *18*, 8398−8405.

57. Sethuraman, V.; McGovern, M.; Morse, D. C.; Dorfman, K. D. Influence of Charge Sequence on the Adsorption of Polyelectrolytes to Oppositely-Charged Polyelectrolyte Brushes. *Soft Matter* **2019**, *15*, 5431−5442.

58. Dahal, U. R.; Wang, Z.; Dormidontova, E. E. Hydration and Mobility of Poly(ethylene oxide) Brushes. *Macromolecules* **2017**, *50*, 6722−6732.

59. Dormidontova, E.; Chen, G. PEO-Grafted Gold Nanopore: Grafting Density, Chain Length, and Curvature Effects. *Macromolecules* **2022**, *55*, 5222−5232.

60. Dahal, U.; Dormidontova, E. Chain Conformation and Hydration of Polyethylene Oxide Grafted to Gold Nanoparticles: Curvature and Chain Length Effect. *Macromolecules* **2020**, *53*, 8160−8170.

61. Sachar, H. S.; Pial, T. H.; Desai, P. R.; Etha, S. A.; Wang, Y.; Chung, P. W.; Das, S. Densely Grafted Polyelectrolyte Brushes Trigger "Water-in-Salt"-like Scenarios and Ultraconfinement Effect. *Matter* **2020**, *2*, 1509−1521.

62. Sachar, H. S.; Pial, T. H.; Chava, B. S.; Das, S. All-atom Molecular Dynamics Simulations of Weak Polyionic Brushes: Influence of Charge Density on the Properties of

Polyelectrolyte Chains, Brush-supported Counterions, and Water Molecules. *Soft Matter* **2020**, *16*, 7808−7822.

63. Pial, T. H.; Sachar, H. S.; Das, S. Quantification of Mono- and Multivalent Counterion-Mediated Bridging in Polyelectrolyte Brushes. *Macromolecules* **2021**, *54*, 4154−4163.
64. Pial, T. H.; Prajapati, M.; Chava, B. S.; Sachar, H. S.; Das, S. Charge-Density-Specific Response of Grafted Polyelectrolytes to Electric Fields: Bending or Tilting? *Macromolecules* **2022**, *55*, 2413−2423.
65. Pial, T. H.; Sachar, H. S.; Desai, P. R.; Das, S. Overscreening, Co-Ion-Dominated Electroosmosis, and Electric Field Strength Mediated Flow Reversal in Polyelectrolyte Brush Functionalized Nanochannels. *ACS Nano* **2021**, *15*, 6507−6516.
66. Sachar, H. S.; Chava, B. S.; Pial, T. H.; Das, S. All-Atom Molecular Dynamics Simulations of the Temperature Response of Densely Grafted Polyelectrolyte Brushes. *Macromolecules* **2021**, *54*, 6342−6354.
67. Pial, T. H.; Das, S. Machine Learning Enabled Quantification of The Hydrogen Bonds Inside the Polyelectrolyte Brush Layer Probed Using All-Atom Molecular Dynamics Simulations. *Soft Matter* **2022**, *18*, 8945−8951.
68. Ishraaq, R.; Akash, T.S; Bera, A.; Das, S. Hydrophilic and Apolar Hydration in Densely Grafted Cationic Brushes and Counterions with Large Mobilities. *J. Phys. Chem. B* **2024**, *128(1)*, 381–392
69. Wu, B.; Wang, X.; Yang, J.; Hua, Z.; Tian, K.; Kou, R.; Zhang, J.; Ye, S.; Luo, Y.; Craig, V. S. J.; et al. Reorganization of Hydrogen Bond Network Makes Strong Polyelectrolyte Brushes Ph-Responsive. *Sci. Adv.* **2016**, *2*, No. 1600579.

70. Chu, X.; Yang, J.; Liu, G.; Zhao, J. Swelling Enhancement of Polyelectrolyte Brushes Induced By External Ions. *Soft Matter* **2014**, *10*, 5568−5578.

71. Jorgensen, W. L.; Maxwell, D. S.; Tirado-Rives, J. Development and Testing of the OPLS All-Atom Force Field on Conformational Energetics and Properties of Organic Liquids. *J. Am. Chem. Soc.* **1996**, *118*, 11225−11236.

72. Joung, I. S.; Cheatham, T. E., III Determination of Alkali and Halide Monovalent Ion Parameters for Use in Explicitly Solvated Biomolecular Simulations. *J. Phys. Chem. B* **2008**, *112*, 9020−9041.

73. Thompson, A. P.; Aktulga, H. M.; Berger, R.; Bolintineanu, D. S.; Brown, W. M.; Crozier, P. S.; in 't Veld, P. J.; Kohlmeyer, A.; Moore, S. G.; Nguyen, T. D.; et al. LAMMPS - A Flexible Simulation Tool For Particle-Based Materials Modeling At The Atomic, Meso, And Continuum Scales. *Comput. Phys. Commun*. **2022**, *271*, No. 108171.

74. Stukowski, A. Visualization and Analysis of Atomistic 904 Simulation Data with OVITO−the Open Visualization Tool. *Model. Simul. Mater. Sci. Eng.* **2010**, *18*, No. 015012.

75. Marcus D Hanwell, M. D.; Curtis, D. E.; Lonie, D. C.; Vandermeersch,T.; Zurek, E. Hutchison, G. R Avogadro: An advanced semantic chemical editor, visualization, and analysis platform. *J. Cheminf.* **2012**, *17*, 4.

76. Jewett, A. I.; Stelter, D.; Lambert, J.; Saladi, S. M.; Roscioni, O. M.; Ricci, M.; Autin, L.; Maritan, M.; Bashusqeh, S. M.; Keyes, T.; Dame, R. T.; Shea, J. M.; Jensen, G. J.; Goodsell, D. S. Moltemplate: A Tool for Coarse-Grained Modeling of Complex Biological Matter and Soft Condensed Matter Physics. *J. Mol. Bio.* **2021**, *433 (11)*, 166841**.**

77. Zhang, Y.; Cremer, P. S. Interactions between Macromolecules and ions: the Hofmeister series. *Curr. Opin. Chem. Biol.* **2006**, *10(6)*, 658-663.

78. Tu, S.; Lobanov, S. S.; Bai, J.; Zhong, H.; Gregerson, J.; Rogers, A. D.; Ehm, L.; John B. Parise, J. B. Enhanced Formation of Solvent-Shared Ion Pairs in Aqueous Calcium Perchlorate Solution toward Saturated Concentration or Deep Supercooling Temperature and Its Effects on the Water Structure. *J. Phys. Chem. B* **2019**, *123(45*), 9654–9667

79. Marcus, Y.; Hefter, G. Ion Pairing. *Chem. Rev.* **2006**, *106(11)*, 4585–4621

80. Yuan, H. ; Liu, G. Ionic Effects on Synthetic Polymers: from Solutions to Brushes and Gels. *Soft Matter*, **2020**, *16*, 4087-4104

81. Moghaddam, S. J.; Thormann, E. The Hofmeister series: Specific ion effects in aqueous polymer solutions *J. Colloid Interface Sci.* **2019**, *555*, 615-635.

82. Mudi, A; Chakravarty, C. Effect of Ionic Solutes on the Hydrogen Bond Network Dynamics of Water: Power Spectral Analysis of Aqueous NaCl Solutions. *J. Phys. Chem. B* **2006**, *110(16*), 8422–8431.

83. Mazzini, V.; Craig, V. S. J. Volcano Plots Emerge from a Sea of Nonaqueous Solvents: The Law of Matching Water Affinities Extends to All Solvents. *ACS Cent. Sci.* **2018**, *4(8)*, 1056–1064

84. Maginn, E. J.; Messerly, R. A; Carlson, D. J.; Roe, D. R.; Elliott, R. Best Practices for Computing Transport Properties 1.Self Diffusivity and Viscosity from Equilibrium Molecular Dynamics *Living Journal of Computational Molecular Science*, **2019**, *1*, 2575-6524

85. Li, Y. H.; Yu, Y.; Qian, J.; Wu, H; Wang, F. C. Anomalous ion transport through angstrom-scale pores: Effect of hydration shell exchange on ion mobility *Appl. Surf. Sci.* **2021**, *560*, 150022